





X-Ray and UV Observations of the Contact Binary KIC 9832227

Dirk Pandel¹  and Lawrence A. Molnar² ¹ Department of Physics, Grand Valley State University, Allendale, MI 49401, USA² Department of Physics & Astronomy, Calvin College, Grand Rapids, MI 49546, USA

Received 2022 August 14; revised 2023 May 25; accepted 2023 June 7; published 2023 July 6

Abstract

We investigate the X-ray and UV emission from the contact binary star KIC 9832227, which was observed with XMM-Newton for one orbital cycle. The binary is detected with an average X-ray luminosity of $3.4 \times 10^{30} \text{ erg s}^{-1}$. The X-ray emission is restricted to energies below 3 keV and originates from a multitemperature plasma with temperatures up to 1 keV. The X-ray spectrum has at least two distinct components, a cooler, mostly steady component, and a hotter component exhibiting significant variability. The variable X-ray emission appears to originate from a compact flare near the contact region between the two stars that is being eclipsed by the secondary. We analyze the eclipse profile to constrain the location, size, and density of the flaring region. The remaining X-ray emission is not eclipsed and could originate from the polar region on the primary star or an extended corona. The UV emission exhibits the same nearly sinusoidal modulation at half the orbital period that is observed at longer wavelengths. The primary and secondary eclipses have slightly different depths, which is generally attributed to starspot activity. Using simulations of the UV light curve with stellar atmosphere models, we deduce the presence of a starspot near the polar region of the primary, and we determine the time of primary eclipse.

Unified Astronomy Thesaurus concepts: Contact binary stars (297); Stellar x-ray flares (1637); X-ray binary stars (1811); Ultraviolet sources (1741); Eclipsing binary stars (444)

1. Introduction

Contact binaries or W Ursae Majoris (W UMa) stars are pairs of eclipsing, nondegenerate stars orbiting so closely that they fill their Roche lobes and share a common envelope. Their orbital periods range from several hours to more than a day. Convection in the shared envelope causes both component stars to have nearly identical surface temperatures, leading to an optical light curve, where the minimum brightness is nearly equal for both eclipses (e.g., Webbink 2003). Many of the known W UMa stars have been observed to be sources of X-ray radiation. Stepień et al. (2001) examined a sample of 102 W UMa stars and found that 57 of them are detected in the ROSAT all-sky survey with X-ray luminosities on the order of $10^{30} \text{ erg s}^{-1}$. The X-ray emission is thought to be related to high levels of chromospheric and coronal activity arising from the shared convective envelope and rapid stellar rotation. However, the X-ray activity observed in W UMa stars is generally weaker than that in other rapidly rotating stars due to a phenomenon referred to as supersaturation. The X-ray luminosity of W UMa stars appears to be correlated with the binary orbital period, with the faster rotating systems being generally weaker X-ray sources (Chen et al. 2006). In some systems, the X-ray emission was found to be variable and exhibit occasional flaring (e.g., McGale et al. 1996).

The origin of the X-ray emission in contact binaries and the specific mechanisms responsible for the emission remain uncertain. In an observation of VW Cep, Gondoin (2004a) detected a steady X-ray flux with only a shallow dip during the primary eclipse and suggested that the X-ray emission arises from an extended corona encompassing both stars. However, Huenemoerder et al. (2006) analyzed high-resolution X-ray

spectra of VW Cep and concluded that the corona is compact and predominantly above the polar regions of the primary star. Understanding the X-ray emission in contact binaries requires extended observations with modern, high-sensitivity instruments. While many W UMa stars have been detected in X-rays (e.g., Geske et al. 2006), most of these detections are from low-sensitivity observations such as the ROSAT all-sky survey, which provide limited information on the variability and spectral properties of the stars. Only a few contact binaries have been observed with sufficient sensitivity and duration to allow for a detailed analysis of their X-ray properties.

In the contact binary VW Cep, Choi & Dotani (1998) observed an X-ray flare lasting ~ 7 hr which was interpreted as a two-ribbon flare occurring on the primary star. A dip in the light curve was identified as an eclipse by the secondary star and used to constrain the size of the flaring region. Another X-ray flare in VW Cep was observed by Gondoin (2004a) and also interpreted as a two-ribbon flare on the primary star. The X-ray spectrum during the flare showed emission at multiple plasma temperatures with the hot component exhibiting much stronger variability than the cool component. A light curve of the nonflaring emission showed only a shallow dip during primary eclipse, indicating that both stars contribute to the X-ray emission. Gondoin (2004b) analyzed an X-ray light curve of 44 Boo and found several shorter flares but no eclipses, suggesting the presence of an extended corona. Singh & Pandey (2022) applied a deconvolution method for eclipsing binaries to the X-ray light curves of 44 Boo and TX Cnc to reconstruct the coronal structures of the component stars. In 44 Boo, both components appear to have highly inhomogeneous coronae with the majority of the X-ray active regions being concentrated toward the poles. In contrast, the coronae in TX Cnc have uniformly distributed X-ray emitting regions with both components being equally active and having the same brightness per surface area. Two other contact binaries, BH Cas (Liu et al. 2019) and 2MASS J11201034–2201340 (Hu et al. 2016) were



Original content from this work may be used under the terms of the [Creative Commons Attribution 4.0 licence](https://creativecommons.org/licenses/by/4.0/). Any further distribution of this work must maintain attribution to the author(s) and the title of the work, journal citation and DOI.

serendipitously detected in unrelated X-ray observations. For both objects no eclipses or significant variability were found, which may, however, be due to the low signal-to-noise ratio of the X-ray light curves. To gain a better understanding of the structure of the X-ray emitting regions in W UMa stars, more dedicated observations with high-sensitivity instruments are needed, in particular of systems where eclipses can be observed in the X-ray light curves. In this paper we report on an XMM-Newton observation of a W UMa star that had not previously been detected in X-rays.

KIC 9832227 is an eclipsing contact binary with an orbital period of 0.458 days. It was originally included in a catalog of RR Lyrae stars (Kinemuchi et al. 2006), but based on Kepler data it was later reclassified as a W UMa star (Kinemuchi 2013). Measurements of the eclipse timing spanning almost two decades showed an exponential decline of the orbital period, which led Molnar et al. (2017) to predict that the binary components would merge into a single star in 2022, resulting in a luminous red nova. However, Socia et al. (2018) analyzed additional eclipse timing data and did not find a significant decline of the orbital period. This discrepancy was attributed to a typographical error, and the binary is no longer expected to merge in the foreseeable future. Molnar et al. (2017) performed a detailed analysis of optical light curves and spectra and determined various system parameters of KIC 9832227. They found a mass ratio $M_2/M_1 = 0.228$, component masses $M_1 = 1.395 M_\odot$ and $M_2 = 0.318 M_\odot$, stellar radii $R_1 = 1.581 R_\odot$ and $R_2 = 0.830 R_\odot$, effective temperatures $T_1 = 5800$ K and $T_2 = 5920$ K, surface gravities $\log g_1 = 4.19$ and $\log g_2 = 4.10$, a fill factor $f = 0.430$, and an orbital inclination $i = 53.19^\circ$. Pavlenko et al. (2018) analyzed infrared spectra obtained during inferior conjunction and determined a similar effective temperature $T_e = 5920$ K and surface gravity $\log g = 4.1$.

In this paper we present an analysis of X-ray and ultraviolet (UV) data of KIC 9832227 obtained with the XMM-Newton space telescope (Jansen et al. 2001). The X-ray properties of the contact binary have not previously been investigated, and this is the first time that X-ray emission is detected from this object. We analyze the X-ray spectrum to determine various spectral parameters, investigate the variability of the X-ray emission, discuss the possible origin of the X-rays, and constrain the properties of the X-ray emitting regions. We also investigate the UV properties of KIC 9832227, simulate the UV light curve using stellar atmosphere models, and determine the time of primary eclipse.

2. Observations

KIC 9832227 was observed with XMM-Newton on 2017 April 18 for one complete orbital cycle of the binary. We obtained 43.6 ks of continuous X-ray data from each of the two EPIC MOS cameras (Turner et al. 2001) and 42.0 ks from the EPIC PN camera (Strüder et al. 2001). Because of the high particle background near the end of the observation, we excluded the last 2.7 ks of the PN data from our analysis. All three cameras were operated in full frame imaging mode. The medium blocking filters were used for the MOS cameras and the thin blocking filter for the PN camera. The data were filtered to include only good X-ray events with patterns 0–12 for MOS and 0–4 for PN.

A prominent X-ray source is detected at coordinates R. A. = $19^{\text{h}}29^{\text{m}}15^{\text{s}}.88$ and decl. = $+46^\circ37'20''.0$ (J2000.0, uncertainty $0''.23$ statistical and $0''.38$ systematic), which is

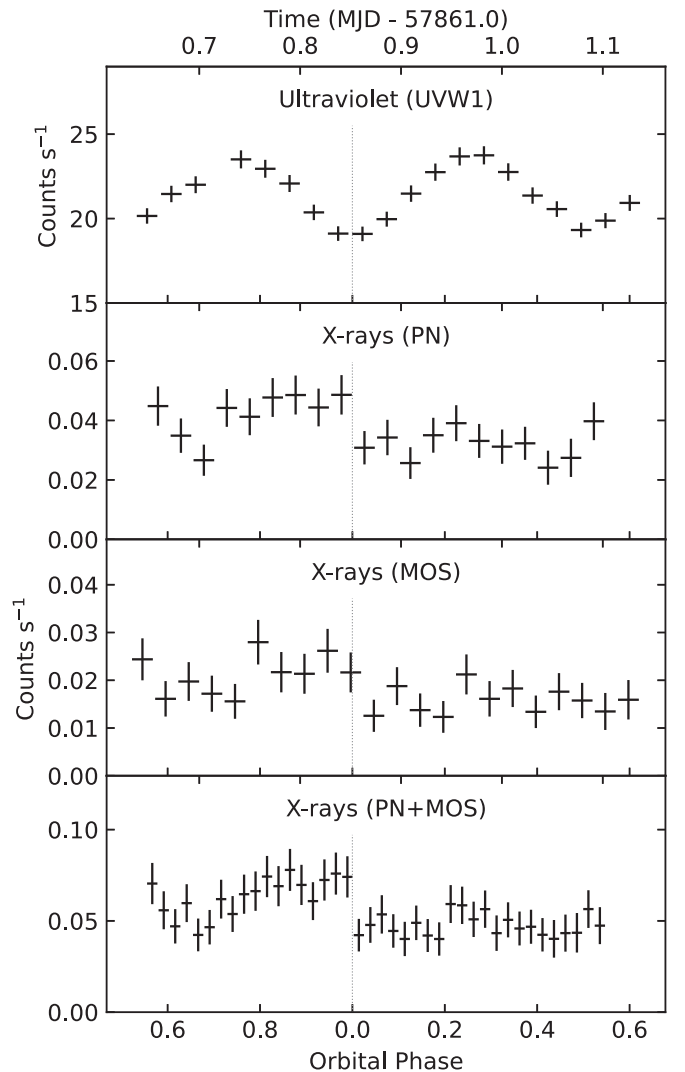


Figure 1. UV and X-ray light curves for the entire XMM-Newton observation. Shown are the UV count rates detected with the Optical Monitor using the UVW1 filter (effective wavelength 291 nm) as well as the individual and combined X-ray count rates detected with the PN and MOS cameras in the 0.3–3.0 keV energy range. The count rates have been corrected for background, aperture size, and various detector inefficiencies. Error bars represent 1σ statistical uncertainties. The dotted line shows the time of orbital phase zero when the primary is at superior conjunction and eclipsed by the secondary which was predicted by the ephemeris in Molnar et al. (2017) to occur at MJD 57861.852.

consistent with the location of KIC 9832227. X-ray events from the source were extracted using a $20''$ circular aperture around this location, and background events were extracted using a larger region on the same CCD with prominent X-ray sources being excluded. Because KIC 9832227 does not emit detectable amounts of high-energy X-rays, we included in our analysis only X-ray events in the energy range 0.3–3.0 keV. KIC 9832227 is detected with a total of ~ 270 X-ray photons in each of the MOS cameras and ~ 880 photons in the PN camera. This corresponds to a combined average EPIC count rate of 0.055 photons s^{-1} when corrected for aperture size and various detector inefficiencies. X-ray light curves for the entire XMM-Newton observation are shown in Figure 1. The object was also observed with the reflection grating spectrometers (den Herder et al. 2001), but no significant X-ray emission is detected.

In addition to the X-ray data, we obtained UV data of KIC 9832227 with the XMM-Newton Optical Monitor (Mason et al. 2001). The telescope was operated with the UVW1 filter which has an effective wavelength of 291 nm. The 43 ks long observation was divided into 20 exposures of 1760 s duration separated by gaps of several minutes during which no data were taken. The Optical Monitor was operated in Fast Mode which provides the arrival times of individual photons inside a small region around the target with a 0.5 s time resolution. We used these data to create UV light curves of KIC 9832227 with time bins shorter than the duration of one exposure. We also obtained one image per exposure covering a larger region which we used to estimate the UV background needed for the light-curve calculation. Photon count rates were corrected for background, aperture size, coincidence losses, dead-time effects, and time-dependent detector degradation. KIC 9832227 is detected with a corrected count rate varying between 19 and 24 photons s^{-1} (Figure 1). To determine the conversion factor between count rate and energy flux, we used the spectrum of a 5800 K stellar atmosphere (Castelli & Kurucz 2003), which is appropriate for KIC 9832227. A count rate of 1 photon s^{-1} with the UVW1 filter corresponds to an average flux density of 0.125 mJy or $4.44 \times 10^{-16} \text{ erg cm}^{-2} \text{ s}^{-1} \text{ \AA}^{-1}$ and a total flux in the filter passband of $6.37 \times 10^{-19} \text{ W m}^{-2}$.

For our timing analysis of the X-ray and UV data, we applied a barycentric correction to the photon arrival times and converted all times to Barycentric Dynamical Time BJD(TDB) and then to MJD = BJD - 2400000.5.

3. Analysis and Results

3.1. UV Light Curve

To model the orbital modulation of the UV emission from KIC 9832227, we created a light curve with a bin width of 40 s using the Optical Monitor Fast Mode data. A light curve of the UV flux density with a larger bin width is shown in Figure 2. The UV light curve exhibits a strong modulation at half the orbital period with a profile similar to that observed at longer wavelengths (see Molnar et al. 2017). This is expected as the majority of the UV emission likely has the same photospheric origin. The two eclipses are very wide, which is typical for contact binaries who share a common envelope, and both eclipses have almost the same depth because of the nearly identical temperatures of the component stars.

We used the PHOEBE eclipsing binary modeling software (Prša et al. 2016; Horvat et al. 2018) to simulate the UV light curve observed with XMM-Newton. PHOEBE uses stellar atmosphere models to generate visual spectra of eclipsing binaries at different orbital phases. We adapted the software to allow us to simulate count rates for the XMM-Newton Optical Monitor and estimate parameters by fitting the model light curve to our data using least-square minimization. For the light curve modeling we used the same parameters as Molnar et al. (2017): orbital period $P = 0.4579331$ days, orbital inclination $i = 53^\circ.19$, mass ratio $M_2/M_1 = 0.228$, semimajor axis of the orbit $a = 2.992 R_\odot$, fill factor $f = 0.430$, effective temperatures $T_1 = 5800 \text{ K}$ and $T_2 = 5920 \text{ K}$, reflection coefficient 0.5, gravity brightening coefficient 0.32, and limb darkening coefficient 0.549. For the distance we assumed a value of 633 pc obtained from Gaia parallax measurements (Gaia Collaboration et al. 2023). The only free parameters in our fit were the time of primary eclipse (phase zero) and a scale factor

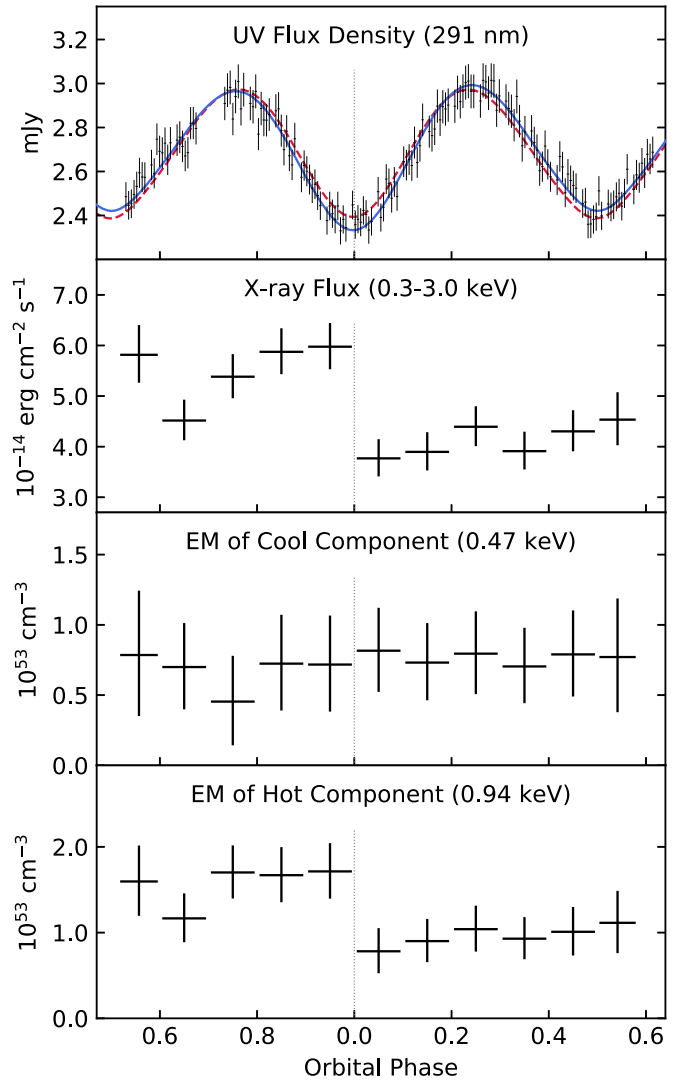


Figure 2. Light curves showing the UV flux density, the X-ray flux, and the emission measures (EM) of the two components in the X-ray spectrum. The top panel shows the flux density in the passband of the UVW1 filter obtained using the Optical Monitor Fast Mode data. For the figure, the data were combined into bins of width 220 s, while smaller 40 s bins were used for model fitting. The red (dashed) curve shows the best fit of a light-curve model without starspots and the blue (solid) curve the best fit of a model with a single starspot on the primary (see Table 1). For the three bottom panels, the X-ray data from all cameras were divided into orbital phase bins of width 0.1 (the first and last bin are slightly smaller due to missing data at the start and end of the observation). For each bin a spectrum was created and fitted with the two-temperature plasma model while keeping all parameters other than the emission measures of the two components fixed at the values shown in Table 2. Error bars represent 1σ statistical uncertainties. Orbital phase zero defines the time when the primary is at superior conjunction and eclipsed by the secondary according to our UV light curve model with a single starspot (see Table 1).

for the UV flux. We were not able to constrain any of the other parameters because of the limited detail of the UV light curve and strong correlations between some parameters.

Our simple model of the binary, with the time of eclipse and flux scale as free parameters and all other parameters fixed at their previously determined values, provides a good fit of the light curve with a reduced chi-square value $\chi_{\text{red}}^2 = 1.21$ (Table 1). However, the light curve shows a small difference between the depths of the two eclipses which is inconsistent with the simple model (dashed curve in Figure 2). This difference is likely caused by the presence of starspots whose

Table 1

System Parameters Obtained by Fitting UV Light-curve Models to the XMM-Newton Optical Monitor Data

Model without Starspots	
MJD of phase zero	57861.8535 ± 0.0011
UV flux scale factor	0.872 ± 0.002
χ^2 value (dof)	1058 (878)
Model with a Single Starspot	
MJD of phase zero	57861.8544 ± 0.0011
UV flux scale factor	0.891 ± 0.003
Starspot on primary:	
Colatitude	25^{+15}_{-10}
Longitude	$15^\circ \pm 15^\circ$
Relative effective temperature	0.88 ± 0.04
Radius	15° (fixed)
χ^2 value (dof)	951 (875)

Note. Phase zero is defined as the time when the primary is at superior conjunction and eclipsed by the secondary (MJD = BJD-2400000.5). For the starspot on the primary, the colatitude is measured from the pole of the primary facing us, the longitude is measured relative to the line connecting the two stars with the angle increasing in the direction of orbital rotation, and the temperature is given relative to the primary’s effective temperature of 5800 K. Uncertainties are shown at 90% confidence. Parameters were estimated using a χ^2 minimization method, and the χ^2 value of the fits as well as the number of degrees of freedom (dof) are shown.

lower temperature leads to a reduced UV flux during orbital phases when a starspot is visible. We therefore extended our model by including a single, circular starspot on the primary star. The starspot is characterized by its location, its effective temperature relative to that of the primary, and its radius. When fitting the light curve, we fixed the radius at a fiducial value of 15° because the parameter is strongly correlated with the relative temperature and cannot be determined independently. This implies that the temperature value we obtained from the fit is not a meaningful estimate of the actual starspot temperature. The model with a single starspot provides a significantly improved fit of the light curve with $\chi^2_{\text{red}} = 1.09$ (solid curve in Figure 2). We find that the starspot is located on the side of the primary facing the secondary at a colatitude of $\sim 25^\circ$ and a longitude of $\sim 15^\circ$. There are likely multiple starspots present, but the resolution of the UV light curve is insufficient to determine the properties of more than one starspot.

As indicated by the UV scale factor, the observed UV flux is lower than that predicted by our model by a factor of 0.89. This discrepancy is likely caused by interstellar extinction. The observed reduction in UV flux corresponds to a total extinction of $A(291 \text{ nm}) = 0.13$. According to the extinction curve by Cardelli et al. (1989), this translates to optical extinction values of $A(V) = 0.067$ and $E(B - V) = 0.022$ assuming the Galactic average of 3.1 for the extinction parameter R_V . Molnar et al. (2017) determined a similar extinction value of $E(B - V) = 0.03(2)$. Taking into account extinction, the observed UV flux at 291 nm is in good agreement with the photospheric emission predict by our model, and we do not find evidence of significant chromospheric UV emission at this wavelength.

3.2. X-Ray Spectrum

To investigate the X-ray spectral properties of KIC 9832227, we combined the data from the three EPIC cameras for the

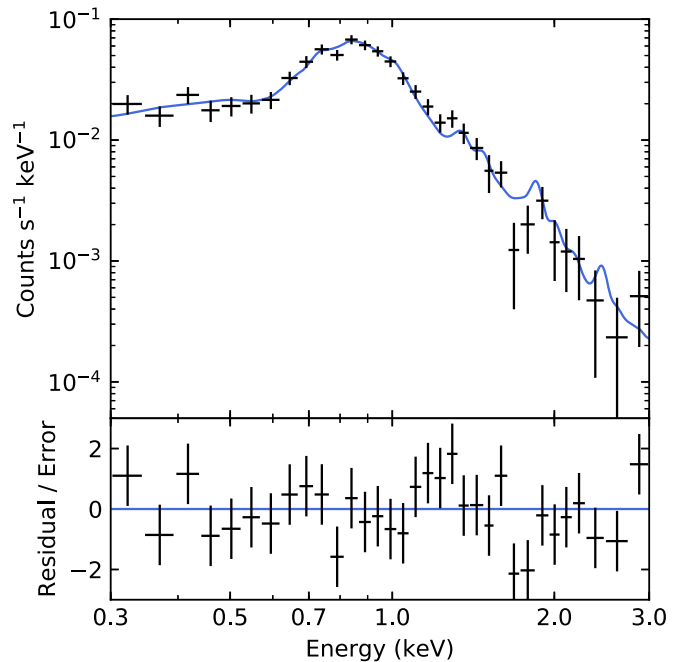


Figure 3. X-ray spectrum showing the combined photon count rates of the three EPIC cameras for the entire XMM-Newton observation. The count rates have been corrected for background, aperture size, and various detector inefficiencies. Error bars represent 1σ statistical uncertainties. The solid line represents our best fit with the multitemperature model (see Table 2). The bottom panel shows the difference between observed and model count rates divided by the statistical error. Note that smaller energy bins than shown here were used for spectral fitting.

entire XMM-Newton observation and created a spectrum of count rate versus photon energy (Figure 3). We then performed spectral fits with various models using XSPEC (Arnaud 1996). The spectrum used for fitting was binned at about one third of the cameras’ energy resolution, which optimizes the counts per bin without removing small spectral features. Because many of the energy bins contain a low number of counts, model parameters were estimated using a maximum likelihood method with C statistic (Cash 1979) rather than χ^2 statistic. As spectral models we used single- and multitemperature versions of the APEC model (Foster et al. 2012) for a collisionally ionized, optically thin gas. We also included in our models photoelectric absorption by neutral gas along the line of sight.

The spectral parameters obtained from our fits are shown in Table 2. We initially used a spectral model with a single plasma temperature, which provides a good fit to the data. The temperature of ~ 0.8 keV obtained from the fit is relatively low, but this is to be expected given the lack of X-ray emission at higher energies. A significant improvement of the C value can be achieved by using a two-temperature model consisting of two distinct single-temperature components. However, adding a third single-temperature component does not further improve the fit, which suggests that the quality of the spectrum is insufficient to distinguish between more than two components. The X-ray emitting gas likely has a continuous temperature distribution whose shape cannot be determined. We therefore fitted the spectrum with a multitemperature model assuming a power-law dependence of the emission measure EM on temperature T given by $dEM/dT \propto T^\alpha$ up to a maximum

Table 2

X-Ray Spectral Parameters Obtained by Fitting Models of a Collisionally Ionized, Optically thin Gas to the XMM-Newton Spectrum of the Entire Observation

Single-temperature Model	
Temperature (keV)	0.78 ± 0.04
Emission measure (10^{53} cm^{-3})	$2.9^{+0.8}_{-0.7}$
Abundance (solar)	$0.25^{+0.09}_{-0.06}$
N_{H} (10^{20} cm^{-2})	$4.5^{+3.4}_{-3.1}$
Flux ($10^{-14} \text{ erg cm}^{-2} \text{ s}^{-1}$)	4.74 ± 0.22
Luminosity ($10^{30} \text{ erg s}^{-1}$)	$3.4^{+0.5}_{-0.4}$
C value (dof)	97.2 (74)
Two-temperature Model	
Component 1:	
Temperature (keV)	$0.47^{+0.20}_{-0.13}$
Emission measure (10^{53} cm^{-3})	$0.9^{+0.7}_{-0.3}$
Component 2:	
Temperature (keV)	$0.94^{+0.20}_{-0.11}$
Emission measure (10^{53} cm^{-3})	$1.5^{+0.9}_{-0.7}$
Abundance (solar)	$0.38^{+0.22}_{-0.14}$
N_{H} (10^{20} cm^{-2})	$4.1^{+5.6}_{-4.1}$
Flux ($10^{-14} \text{ erg cm}^{-2} \text{ s}^{-1}$)	4.72 ± 0.23
Luminosity ($10^{30} \text{ erg s}^{-1}$)	$3.3^{+0.8}_{-0.5}$
C value (dof)	89.5 (72)
Multitemperature Model	
Maximum temperature T_{max} (keV)	$1.02^{+0.24}_{-0.13}$
Power-law index α	$0.9^{+1.7}_{-1.0}$
Emission measure (10^{53} cm^{-3})	$2.4^{+2.1}_{-1.3}$
Abundance (solar)	$0.41^{+0.40}_{-0.15}$
N_{H} (10^{20} cm^{-2})	$4.5^{+4.6}_{-3.9}$
Flux ($10^{-14} \text{ erg cm}^{-2} \text{ s}^{-1}$)	4.72 ± 0.23
Luminosity ($10^{30} \text{ erg s}^{-1}$)	$3.4^{+0.9}_{-0.5}$
C value (dof)	90.7 (73)

Note. Fluxes shown are absorbed and for the energy range 0.3–3.0 keV. Luminosities are unabsorbed, include energies >0.1 keV, and were determined assuming isotropic emission and a distance of 633 pc (Gaia Collaboration et al. 2023). Elemental abundances are relative to the solar values by Asplund et al. (2009). N_{H} is the neutral hydrogen column density along the line of sight. Uncertainties are shown at 90% confidence. Parameters were estimated using a maximum likelihood method with C statistic (Cash 1979), and the C value of the fits as well as the number of degrees of freedom (dof) are shown. The emission measure is the volume integral $\text{EM} = \int n_e n_H dV$ (n_e and n_H are the electron and hydrogen densities) and only includes the visible regions of the X-ray emitting gas. For the multitemperature model, we assumed a power-law distribution of the differential emission measure versus temperature $d\text{EM}/dT \propto T^\alpha$ up to a maximum temperature T_{max} . The emission measure shown is the total over the entire temperature range.

temperature T_{max} . This multitemperature model fits the data equally well as the two-temperature model (Table 2).

From our spectral fits, we obtained an average X-ray luminosity $L_X = 3.4 \times 10^{30} \text{ erg s}^{-1}$ (>0.1 keV) after taking into account interstellar absorption and assuming isotropic emission. This is consistent with the X-ray luminosities of other W UMa stars with a similar orbital period, which are in the range $0.5\text{--}10 \times 10^{30} \text{ erg s}^{-1}$ (Chen et al. 2006). From optical observations, Molnar et al. (2017) determined a bolometric luminosity $L_{\text{bol}} = 1.3 \times 10^{34} \text{ erg s}^{-1}$, which implies a luminosity ratio $\log(L_X/L_{\text{bol}}) = -3.6$. This ratio is within the range found by Stępień et al. (2001) for other W UMa stars

with a similar orbital period and color index ($B - V \approx 0.6$). Like for most W UMa stars, the level of X-ray activity in KIC 9832227 is significantly lower than that of other rapidly rotating stars. This phenomenon is referred to as super-saturation (see e.g., Stępień et al. 2001; Chen et al. 2006).

The neutral hydrogen column density $N_{\text{H}} \approx 4 \times 10^{20} \text{ cm}^{-2}$ is less than the total galactic value $N_{\text{H}} = 8.0 \times 10^{20} \text{ cm}^{-2}$ in the direction of KIC 9832227 (HI4PI Collaboration et al. 2016). Our estimate of N_{H} is consistent with the extinction value $A(V) = 0.20$ we obtained from the UV light curve (Section 3.1). For this extinction, the relationship by Güver & Özel (2009) predicts a column density $N_{\text{H}} = 4.4 \times 10^{20} \text{ cm}^{-2}$, which is well within the uncertainty of our estimate from the X-ray spectral fit.

3.3. X-Ray Light Curve

A light curve of the combined X-ray count rates of the three EPIC cameras is shown in Figure 1. The light curve exhibits significant differences between the first and second halves of the observation, with the first half showing stronger variability and an up to 50 per cent higher count rate. We investigated this variability using a Bayesian Blocks method (Scargle et al. 2013) to find statistically significant changes of the X-ray flux. We detect two distinct features in the light curve, a broad dip near the beginning of the observation and a sudden drop near the midpoint. All other apparent fluctuations visible in the light curve are not statistically significant.

To investigate variations of the X-ray spectrum, we divided the data from the three cameras into time bins of width 0.1 based on orbital phase and created a spectrum for each phase bin. We then fitted each of the spectra with the same two-temperature plasma model that was used with the spectrum of the entire observation (see Section 3.2), but because of the lower signal-to-noise ratio, we only varied the emission measures of the two components while keeping the other parameters fixed at the values shown in Table 2. The total X-ray flux and the two emission measures versus orbital phase are shown in Figure 2.

The light curve of the X-ray flux in Figure 2 clearly shows the two features we found using the Bayesian Blocks method, a broad dip around phase 0.6–0.7 and a sudden drop near phase 0.0. The elevated flux during the first half of the observation was predominantly caused by a larger emission measure of the hotter (0.94 keV) component in our two-temperature model, while the cooler (0.47 keV) component appears to be mostly constant throughout the entire observation. This suggests that the excess emission during the first half originated from a distinct region with a higher plasma temperature. It is not clear whether the higher flux at phase 0.6–0.0 was a short-term flaring event or a repeating feature in the light curve as the XMM-Newton observation only covered slightly more than one orbital cycle. However, the elevated flux at phase 0.5–0.6 at the beginning of the observation could be attributed to a short-term flare since the flux is significantly lower at the same phase one orbital cycle later.

X-ray variability in contact binaries can generally be attributed to either stellar flares or the eclipsing of X-ray emitting regions near the surface of the stars. The elevated flux and higher plasma temperature at phase 0.6–0.0 could have been caused by a stellar flare lasting at least 4 hr. However, stellar flares are generally characterized by a rapid rise of the X-ray flux and a slow decline due to the cooling of the plasma.

This is inconsistent with the rapid decline we observe near phase 0.0. Given the duration and intensity of the flare, a much more gradual decline would be expected. It is reasonable to conclude that the elevated flux at phase 0.6–0.0 originated from a compact X-ray emitting region that was being eclipsed near phase 0.0. In Section 3.1 we inferred from the UV light curve the presence of a starspot at 25° colatitude on the primary. The active region above the starspot could have been contributing significantly to the X-ray emission. However, for the orbital inclination of the system, a starspot at this colatitude is never eclipsed, and the X-ray emission from the optically thin plasma above the starspot is isotropic. Therefore, any X-ray emission from the starspot region is not expected to exhibit variability due to the orbital motion. The elevated flux during the first half of the observation must have originated from a different region at a higher colatitude that can be eclipsed.

Assuming that the elevated X-ray flux originated from a compact region on the primary star, such as a stellar flare, it is possible to constrain the location and size of the region. We fitted the light curve around phase 0.0 with the model of a circular X-ray emitting region on the primary that is being eclipsed by the secondary. To better constrain the eclipse profile, we used a small bin width of 100 s and applied a maximum likelihood method to account for the low number of counts in each bin. We obtained a best-fit value for the time of the eclipse (i.e., when half of the region is eclipsed by the secondary) of phase 0.991 with a 90% confidence range of 0.980–0.006. The X-ray count rate was insufficient to resolve the profile of the eclipse, but we were able to obtain an upper limit of 15° or 3×10^{10} cm on the diameter of the region. Given the orbital inclination of the system, the presence and timing of the eclipse places strong constraints on the location of the X-ray emitting region. We estimate that the region was located at a colatitude of $\sim 110^\circ$ and a longitude of $\sim 25^\circ$, which is near the contact region between the two stars. At a lower colatitude we would not observe an eclipse by the secondary, and at a higher colatitude the region would always be hidden behind the primary. For the location we determined, the region would be eclipsed until phase 0.7 when it moves over the limb of the primary and becomes visible again. This is consistent with the increase of the X-ray flux observed near phase 0.7 and the lower flux during the second half of the observation.

From the light-curve fit we also determined that the compact region had an X-ray luminosity of 1.2×10^{30} erg s $^{-1}$ and an emission measure of 8.2×10^{52} cm $^{-3}$. This luminosity is 10^2 – 10^3 times higher than that of a typical 2-ribbon solar flare. The emission measure EM is related to the volume V and the average electron density n by $EM = n^2 V$. We used our upper limit of 3×10^{10} cm for the diameter of the X-ray emitting region to derive a lower limit for the density. We assumed that the X-ray emission originated from a stellar flare with a cylindrical shape. Since the flare is eclipsed by the secondary, its height is limited by the space between the two stars and must be less than about 1 solar radius. Using these constraints for the width and height of the flare we obtained a lower limit of $n > 4 \times 10^{10}$ cm $^{-3}$ for the electron density.

X-ray flaring activity has been reported for several other contact binaries. Choi & Dotani (1998) observed a flare in VW Cep that lasted ~ 7 hr and was characterized by a rapid rise of the X-ray flux and a slow, exponential decline. It was interpreted as a two-ribbon flare occurring on the primary star. The flare had a peak luminosity of $\sim 1.2 \times 10^{30}$ erg s $^{-1}$, very

similar to what we found for KIC 9832227. A dip in the X-ray light curve was identified as an eclipse of the flaring region by the secondary star. The electron density of the flare was estimated to be $\sim 5 \times 10^{10}$ cm $^{-3}$, which is close to our lower limit for the flare in KIC 9832227. Another flare in VW Cep was observed by Gondoin (2004a) and also interpreted as a two-ribbon flare on the primary star. The hot component in the X-ray spectrum exhibited much stronger variability during the flare than the cool component, similar to what we observed for KIC 9832227 (Figure 2). The flare had an X-ray luminosity of $\sim 2 \times 10^{30}$ erg s $^{-1}$ and an electron density $> 6.5 \times 10^{10}$ cm $^{-3}$. In the contact binary 44 Boo, Gondoin (2004b) observed several smaller and shorter flares lasting ~ 0.5 hr each.

In another observation of VW Cep, Gondoin (2004a) detected a steady X-ray flux with only a shallow dip during the primary eclipse. They concluded that both stars contribute to the X-ray emission and that the emission could arise from an extended corona encompassing the two companions. However, Huenemoerder et al. (2006) concluded based on high-resolution X-ray spectra of VW Cep that the corona is compact and predominantly above the polar regions of the primary star. Either of these scenarios is consistent with our findings for KIC 9832227 if we exclude the X-ray emission from the eclipsed, compact region discussed above. The remaining emission, as represented by the cool component shown in Figure 2, does not exhibit significant variability. For the high 53° orbital inclination of KIC 9832227, any X-ray emission from the polar regions on the primary would not show an orbital modulation or an eclipse by the secondary because one of the poles is always visible while the other is always obscured. Similarly, an extended corona around the two stars would not result in a significant orbital modulation of the X-ray flux. The starspot we inferred from the UV light curve (see Section 3.1) is close to the unobscured pole, and it may be a major contributor to the steady X-ray emission.

3.4. Eclipse Timing

Socia et al. (2018) obtained optical light curves of the contact binary 45 days after the XMM-Newton observation. Based on their measurements of eclipse timing and orbital period (0.4579515 days), we can extrapolate that the primary eclipse should have occurred during the XMM-Newton observation at MJD 57861.8522. This agrees to within 2σ (3 min) with our measurement of MJD 57861.8544. Small fluctuations of the eclipse timing are not unusual. Deviations of as much as 10 minutes over timescales of tens of days have been observed for KIC 9832227 (Figure 1; Socia et al. 2018). They are possibly caused by starspots that rotate slightly asynchronously and distort the eclipse profile. Socia et al. (2018) also found that the eclipse occurred 40 minutes earlier than predicted by a linear ephemeris based on previous observations. This discrepancy is too large to be attributed to starspots and indicates a real change in orbital period. Kovacs et al. (2019) analyzed additional eclipse timing data and found that it strongly supports the presence of a distant low-mass companion star with an orbital period of ~ 13.5 yr.

4. Summary

In contact binaries the shared convective envelope and rapid stellar rotation causes enhanced chromospheric and coronal activity resulting in higher levels of X-ray emission compared

to other stars. KIC 9832227 is found to be a strong X-ray source with a luminosity comparable to that of other contact binaries with similar orbital periods. The X-ray emission originates from a multitemperature plasma with temperatures up to ~ 1 keV. Although the X-ray emitting gas likely has a continuous temperature distribution, we were only able to distinguish two components in the spectrum. The cooler component is mostly steady throughout the orbital cycle and does not appear to be eclipsed. However, the hotter component exhibits significant variability, and part of this emission appears to originate from a compact flare that is being eclipsed by the secondary star. The flare, which is 10^2 – 10^3 times brighter in X-rays than a typical solar flare, is located near the contact region between the two stars. The profile of the eclipse by the secondary is not resolved, but we were able to determine an upper limit for the size of the flare and a lower limit for its density.

Unlike the X-ray emission, the UV emission originates mostly from the photosphere and exhibits the same nearly sinusoidal modulation that is seen at longer wavelengths. The UV light curve is well described by modeling the photospheric emission while taking into account the mutual eclipsing of the stars. Because of the common envelope and the nearly identical temperatures of the component stars, the primary and secondary eclipses are very wide and are expected to have the same depth. However, we find a small asymmetry between the two eclipses which we attribute to a starspot near the unobscured polar region of the primary star. The starspot is not eclipsed and may be a major contributor to the steady X-ray emission.

The X-ray emission from contact binaries has been suggested to originate either from the polar regions on the primary or an extended corona encompassing both stars. Given the high orbital inclination of KIC 9832227, both scenarios could explain the steady X-ray emission we observe. However, our analysis demonstrates that compact flares near the contact region between the two stars can contribute significantly to the X-ray emission from W UMa stars.

Acknowledgments

This work was supported by NASA under award number 80NSSC18K0610 and is based on observations obtained with XMM-Newton, an ESA science mission with instruments and contributions directly funded by ESA member states and NASA.

Facility: XMM-Newton.

Software: XMM-Newton SAS (Gabriel et al. 2004), XSPEC (Arnaud 1996), PHOEBE (Prša et al. 2016; Horvat et al. 2018).

ORCID iDs

Dirk Pandel  <https://orcid.org/0000-0003-2085-5586>

Lawrence A. Molnar  <https://orcid.org/0000-0002-5472-4181>

References

- Arnaud, K. A. 1996, in ASP Conf. Ser., Vol. 101, *Astronomical Data Analysis Software and Systems V*, ed. G. H. Jacoby & J. Barnes (San Francisco, CA: ASP), 17
- Asplund, M., Grevesse, N., Sauval, A. J., & Scott, P. 2009, *ARA&A*, 47, 481
- Cardelli, J. A., Clayton, G. C., & Mathis, J. S. 1989, *ApJ*, 345, 245
- Cash, W. 1979, *ApJ*, 228, 939
- Castelli, F., & Kurucz, R. L. 2003, in IAU Symp. 210, *Modelling of Stellar Atmospheres*, ed. N. Piskunov, W. W. Weiss, & D. F. Gray (Cambridge: Cambridge Univ. Press), A20
- Chen, W. P., Sanchawala, K., & Chiu, M. C. 2006, *AJ*, 131, 990
- Choi, C. S., & Dotani, T. 1998, *ApJ*, 492, 761
- den Herder, J. W., Brinkman, A. C., Kahn, S. M., et al. 2001, *A&A*, 365, L7
- Foster, A. R., Ji, L., Smith, R. K., & Brickhouse, N. S. 2012, *ApJ*, 756, 128
- Gabriel, C., Denby, M., Fyfe, D. J., et al. 2004, in ASP Conf. Ser., Vol. 314, *Astronomical Data Analysis Software and Systems XIII*, ed. F. Ochsenbein, M. G. Allen, & D. Egret (San Francisco, CA: ASP), 759
- Geske, M. T., Gettel, S. J., & McKay, T. A. 2006, *AJ*, 131, 633
- Gondoin, P. 2004a, *A&A*, 415, 1113
- Gondoin, P. 2004b, *A&A*, 426, 1035
- Güver, T., & Özel, F. 2009, *MNRAS*, 400, 2050
- Gaia Collaboration, Vallenari, A., Brown, A. G. A., et al. 2023, *A&A*, 674, A1
- Horvat, M., Conroy, K. E., Pablo, H., et al. 2018, *ApJS*, 237, 26
- Hu, C.-P., Yang, T.-C., Chou, Y., et al. 2016, *AJ*, 151, 170
- Huenemoerder, D. P., Testa, P., & Buzasi, D. L. 2006, *ApJ*, 650, 1119
- HI4PI Collaboration, Ben Bekhti, N., Flöer, L., et al. 2016, *A&A*, 594, A116
- Jansen, F., Lumb, D., Altieri, B., et al. 2001, *A&A*, 365, L1
- Kinemuchi, K. 2013, arXiv:1310.0544
- Kinemuchi, K., Smith, H. A., Woźniak, P. R., McKay, T. A. & ROTSE Collaboration 2006, *AJ*, 132, 1202
- Kovacs, G., Hartman, J. D., & Bakos, G. Á. 2019, *A&A*, 631, A126
- Liu, J., Esamdin, A., Zhang, Y., et al. 2019, *PASP*, 131, 084202
- Mason, K. O., Breeveld, A., Much, R., et al. 2001, *A&A*, 365, L36
- McGale, P. A., Pye, J. P., & Hodgkin, S. T. 1996, *MNRAS*, 280, 627
- Molnar, L. A., Van Noord, D. M., Kinemuchi, K., et al. 2017, *ApJ*, 840, 1
- Pavlenko, Y. V., Evans, A., Banerjee, D. P. K., et al. 2018, *A&A*, 615, A120
- Prša, A., Conroy, K. E., Horvat, M., et al. 2016, *ApJS*, 227, 29
- Scargle, J. D., Norris, J. P., Jackson, B., & Chiang, J. 2013, *ApJ*, 764, 167
- Singh, G., & Pandey, J. C. 2022, *ApJ*, 934, 20
- Socia, Q. J., Welsh, W. F., Short, D. R., et al. 2018, *ApJL*, 864, L32
- Stepień, K., Schmitt, J. H. M. M., & Voges, W. 2001, *A&A*, 370, 157
- Strüder, L., Briel, U., Dennerl, K., et al. 2001, *A&A*, 365, L18
- Turner, M. J. L., Abbey, A., Arnaud, M., et al. 2001, *A&A*, 365, L27
- Webbink, R. F. 2003, in ASP Conf. Ser., Vol. 293, *3D Stellar Evolution*, ed. S. Turcotte, S. C. Keller, & R. M. Cavallo (San Francisco, CA: ASP), 76